

Article

Enhancing Part-to-Part Repeatability of Force-Sensing Resistors Using a Lean Six Sigma Approach

Andrés O. Garzón-Posada^{1,2}, Leonel Paredes-Madrid^{1,*} , Angela Peña³, Victor M. Fontalvo¹ and Carlos Palacio⁴ 

¹ Faculty of Engineering, Universidad Católica de Colombia, Carrera 13 # 47-30, Bogota 110221, Colombia; aogarzon@ucatolica.edu.co (A.O.G.-P.); vmfontalvo@ucatolica.edu.co (V.M.F.)

² Department of Applied Physics, Materials and Surface Lab (Nanotechnology Unit), Faculty of Sciences, Universidad de Málaga, ES29071 Malaga, Spain

³ Faculty of Mechanical, Biomedical and Electronic Engineering, Universidad Antonio Nariño, Carrera 7 # 21-84, Tunja 150001, Colombia; angelapena@uan.edu.co

⁴ GIFAM Group, Faculty of Sciences, Universidad Antonio Nariño, Carrera 7 # 21-84, Tunja 150001, Colombia; carlospalacio@uan.edu.co

* Correspondence: ljparedes@ucatolica.edu.co; Tel.: +57-(1)-327-7300

Abstract: Polymer nanocomposites have found wide acceptance in research applications as pressure sensors under the designation of force-sensing resistors (FSRs). However, given the random dispersion of conductive nanoparticles in the polymer matrix, the sensitivity of FSRs notably differs from one specimen to another; this condition has precluded the use of FSRs in industrial applications that require large part-to-part repeatability. Six Sigma methodology provides a standard framework to reduce the process variability regarding a critical variable. The Six Sigma core is the DMAIC cycle (Define, Measure, Analyze, Improve, and Control). In this study, we have deployed the DMAIC cycle to reduce the process variability of sensor sensitivity, where sensitivity was defined by the rate of change in the output voltage in response to the applied force. It was found that sensor sensitivity could be trimmed by changing their input (driving) voltage. The whole process comprised: characterization of FSR sensitivity, followed by physical modeling that let us identify the underlying physics of FSR variability, and ultimately, a mechanism to reduce it; this process let us enhance the sensors' part-to-part repeatability from an industrial standpoint. Two mechanisms were explored to reduce the variability in FSR sensitivity. (i) It was found that the output voltage at null force can be used to discard noncompliant sensors that exhibit either too high or too low sensitivity; this observation is a novel contribution from this research. (ii) An alternative method was also proposed and validated that let us trim the sensitivity of FSRs by means of changing the input voltage. This study was carried out from 64 specimens of Interlink FSR402 sensors.

Keywords: nanocomposites; tactile sensors; force sensors; pressure sensors; sensor phenomena and characterization; regression analysis; Gaussian distribution



Citation: Garzón-Posada, A.O.; Paredes-Madrid, L.; Peña, A.; Fontalvo, V.M.; Palacio, C. Enhancing Part-to-Part Repeatability of Force-Sensing Resistors Using a Lean Six Sigma Approach. *Micromachines* **2022**, *13*, 840. <https://doi.org/10.3390/mi13060840>

Academic Editor: Kazunori Hoshino

Received: 25 February 2022

Accepted: 22 May 2022

Published: 27 May 2022

Publisher's Note: MDPI stays neutral with regard to jurisdictional claims in published maps and institutional affiliations.



Copyright: © 2022 by the authors. Licensee MDPI, Basel, Switzerland. This article is an open access article distributed under the terms and conditions of the Creative Commons Attribution (CC BY) license (<https://creativecommons.org/licenses/by/4.0/>).

1. Introduction

Force-sensing resistors (FSRs) are typically manufactured from a blend of an insulating polymer with conductive nanoparticles ([1–6]. The resulting nanocomposite exhibits a piezoresistive response that can be used to either measure compressive forces [6] or tensile loads [3,4,7]. Given the low profile and low cost of FSRs, their usage in research and industrial applications is currently increasing [8]. Multiple studies related to gait analysis [9–11], robotics [12,13], and other disciplines have reported the usage of polymer nanocomposites to perform strain/stress measurements [14–17].

In recent years, there has been an explosion in the number of studies that have developed novel techniques for manufacturing conductive polymers composites (CPCs). Recent studies have incorporated conductive polymers as a replacement for conductive

particles [18–20]; this is a desirable characteristic given the toxicity of graphene, carbon nanotubes (CNTs), and carbon black (CB) [21]. Similarly, the introduction of self-healing properties to the nanocomposite has been also studied by multiple authors [22–24]. Previous authors' works have mainly focused on: first, improving the performance of FSRs by studying the effect of source voltage in the repeatability of measurements [25], and second, developing tailored driving circuits that can help us to minimize time drift and electrical hysteresis [26].

Despite the previously mentioned efforts, the overall performance of FSRs and CPCs still lags behind that of load cells performance in multiple ways. By comparing commercial FSRs [27–29] with an LCHD-5 load cell from Omega Engineering (Norwalk, CT, USA) [30], a difference of up to two orders of magnitude is evident in the metrics of hysteresis and accuracy. Fortunately, studies from Urban et al. [31] and Nguyen and Chauban [32] have helped to narrow the performance gap between both sensing technologies. However, one of the most important drawbacks of FSRs, which has not been yet addressed by specific literature, is the inability to know sensor sensitivity a priori. Given the random dispersion of conductive nanoparticles along the insulating polymer matrix [33], it is not possible to determine the resulting sensitivity of a given nanocomposite, i.e., every specimen has a different sensitivity. This characteristic limits the extensive usage of FSRs since individual sensor calibration is required before use. This condition is not a major concern when only a few sensors are required in the final application, but when multiple sensors are required, sensor characterization is a time-consuming task; ultimately, a more suitable sensing technology may be preferred instead. Robotic skins and tactile pads are representative examples of applications requiring multiple sensing points. In these types of deployments, sensor arrays with multiple tactels are employed to detect shapes and force profiles [34].

As pointed out by Castellanos-Ramos et al., the characterization of piezoresistive tactile pads required a complex test bench with an air compressor and tailored hardware; this was performed to match the specific dimensions of the tactile pad [34]. The aim of this study is to develop techniques that save time and resources by avoiding individual sensor calibration. In this research, we address such a concern by using the Lean Six Sigma Methodology (LSSM) to a group of 64 specimens of commercial FSRs, manufactured by Interlink Electronics, Inc. (Westlake Village, CA, USA) [27].

It must be stated that the application of the LSSM to FSRs represents a novelty. By looking up the following keyword combinations in the Scopus search engine without year constraints: Six Sigma and FSR, Six Sigma and polymer composite, Six Sigma and piezoresistive sensor, a total of 68 entries were found. Most of the entries found were inaccurate because Sigma is used to designate sensors' sensitivity. Only six studies truly reported the use of LSSM [35–40], but most of them reported calibration procedures for pressure-sensing equipment in automotive applications.

The rest of this paper is organized as follows: Section 2 briefly describes the theoretical foundations of the Lean Six Sigma methodology and the physical modeling of FSRs, the experimental setup for gathering sensor data is described in Section 3, followed by the application of the LSSM in Section 4. Conclusions are addressed in Section 5.

2. Theoretical Foundations

2.1. Application of the Six Sigma Methodology

Readers may refer to Appendix A for a theoretical description of the Lean Six Sigma methodology (LSSM). In this section, we describe the application of the LSSM to our study case. The goal of this research is to reduce the sensitivity dispersion of FSRs by adjusting their driving voltage and/or by discarding noncompliant sensors. As previously mentioned, the reduction in sensitivity dispersion avoids individual sensor calibration, which ultimately saves time and resources.

In order to reduce sensitivity dispersion, we have deployed the core of the LSSM, i.e., the DMAIC cycle (Define, Measure, Analyze, Improve, and Control). The Six Sigma methodology can be implemented during any phase of product development, manufac-

turing, and later deployment into the final application [41]. The current research only considered the application of the LSSM to reduce FSR variability, as measured from their sensitivity; this is known in industry as the enhancing of part-to-part repeatability [27]. In this study, we only considered compensation techniques into the last stage of final application deployment. However, several authors have explored different methods during sensor fabrication, such as addition of surfactants [42] and the application of magnetic fields to reduce the percolation threshold [43]. Given the fact that we only applied compensation techniques into the last stage of final application deployment, the ultimate goal of Six Sigma reduction was partially achieved.

In order to obtain a Six Sigma reduction in sensitivity dispersion, it is required to apply the DMAIC cycle from the reception of raw materials, followed by rigorous control of sensor manufacturing and assembly; this whole process, although possible, would require separate research.

In this study, the DMAIC was deployed by measuring the output voltage at null force (U_o^{0N}) for each sensor as received from the manufacturer. Later, we correlated U_o^{0N} with sensor sensitivity and developed a statistical model to trim the driving voltage of the FSRs; this process required a thorough understanding of the sensing mechanism of FSRs, which are discussed in Section 2.2. Specific details of the DMAIC cycle are later addressed in Section 4.

2.2. Physical Modeling of Force-Sensing Resistors

Multiple authors have studied the underlying physics of CPCs under different mechanical and electrical conditions, such as compressed/uncompressed operation [44–46], sourcing at low/high voltages [47,48], and finite element analysis by considering changes in particle dimension and spatial distribution [49,50]. The aforementioned studies agree on the fact that piezoresistivity mainly originates from two phenomena: quantum tunneling occurring among adjacent conductive particles separated by the insulating polymer, and constriction resistance occurring at clusters of multiple particles. Each phenomenon is subsequently described.

2.2.1. Quantum Tunneling as a Source of Piezoresistivity

This conduction mechanism can be explained from widely known equations by Simmons that describe the tunneling current between electrodes separated by a thin insulating film [51]. When operating at voltages near zero, a tunneling barrier of thickness (s), with an input applied voltage (U), exhibits a current density (J) equal to:

$$J(U, s) = \frac{3e^2\sqrt{2mV_a}}{2h^2s} U \exp\left(-\frac{4\pi s}{h}\sqrt{2mV_a}\right) \quad (1)$$

where (h) is the Planck constant, (V_a) is the height of the insulating potential barrier and (m), (e) are the electron mass and charge, respectively. However, if $U \gg V_a/e$, the current density can be obtained from the following expression:

$$J(U, s) = \frac{2.2e^3U^2}{8\pi hV_a s^2} \exp\left(-\frac{8\pi s}{2.96heU}\sqrt{2mV_a^3}\right) \quad (2)$$

For the sake of this paper, the full set of equations for the intermediate voltage ranges are not presented since they are not required, but they can be found in the original study from Simmons [51]. Note that regardless of the applied voltage, U , current density changes in a negative exponential fashion with the interparticle separation, i.e., this observation also holds for the intermediate voltage equations not included in this study. Similarly, when operating at high input voltages, a change in U impacts current density (and also the

sensor's sensitivity) in a nonlinear fashion. Under a compression regime, it is possible to relate s with the external applied force (F) as next:

$$s(F) = s_0(1 - F/(AM)) \quad (3)$$

where (s_0) is the uncompressed interparticle separation, (A) is the sensor area, and (M) is the compressive modulus of the nanocomposite. It is possible to substitute (3) into (1) and (2) to obtain unified equations that relate current density with the external applied force.

Figure 1 shows the tunneling phenomenon occurring in multiple spots along the nanocomposite. In practice, the net tunneling resistance (R_{tum}) is originated from the multiple parallel and series connections that occur in the 3D polymer matrix. Unfortunately, an explicit expression for R_{tum} can only be found for voltages near zero using (1), but when $U \gg V_a/e$, an explicit relationship for U/J cannot be found since U appears as part of the argument in the exponential function, see (2).

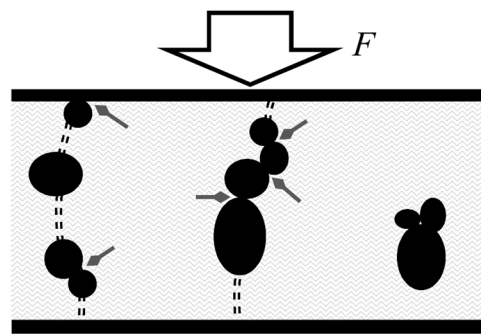


Figure 1. Sketch of a nanocomposite comprising randomly spaced conductive particles in an insulating polymer matrix; the material is sandwiched between metallic electrodes and subjected to an external compressive force (F). Quantum tunneling conduction is shown as double dashed line paths; they connect isolated particles, thus creating the tunneling resistance. Greyed diamond arrows mark the constriction resistance occurring between adjacent particles (as well as between electrode and particles in contact); they create the constriction resistance (R_c). Particles located too far from each other fail to create a conduction path.

For most CPCs involving conductive nanoparticles, the height of the potential barrier is, at most, 0.57 eV for a Sn–Pb/PS nanocomposite [52], where PS stands for polystyrene. Later, in Section 4, we demonstrate that the optimal operating range for the Interlink sensors is accessible for voltages around 3 V. By taking the largest case of $V_a = 0.57$ eV, we can straightforwardly discard (1) as a valid model since it only holds for voltages near 0 V. On the other hand, Equations (2) and (3) are better suited to modeling the piezoresistive response of Interlink sensors when predominantly operating under quantum tunneling regime; this occurs because (2) holds when $U \gg V_a/e$, which is the working case since U is around 3 V and $V_a = 0.57$ eV.

Finally, it must be clarified that current density can be converted to current by considering the effective tunneling area. Nonetheless, the effective tunneling area is not the same as the sensor area, A , because electrons flow only through some regions of the polymer with high particle concentration; see Figure 1. A comprehensive discussion of Simmons's equations for modeling piezoresistive sensors was performed by the authors in a previous study [25]. Such study experimentally determined the effective tunneling area, as well as the whole set of parameters considered in (1)–(3).

2.2.2. Constriction Resistance as a Source of Piezoresistivity

The constriction resistance (R_c) originates at two different spots: first, at the incomplete percolation paths located along the polymer matrix; these are the particle-particle interactions, and second, at the sensor boundary where electrode-particle interactions occur; both cases are shown in Figure 1. For particles with diameters ranging from a hundred

nanometers to tens of micrometers, the contact size is comparable with the mean free path of electrons, thus causing a restriction to free electron motion [53]. According to the model developed by Mikrajuddin et al. [54], when operating under compression regime, the constriction resistance changes in an inversely proportional fashion with the applied force:

$$R_c(F) \propto R_o/F \quad (4)$$

The constant (R_o) depends on the particles physical dimensions, Poisson ratio of the material, and elasticity modulus. For simplicity purposes, the exact expression is not presented here as it comprises a piecewise function for the elastic and inelastic interaction occurring at the interface; such an explanation falls out the scope of this article. However, we must emphasize that the constriction resistance is a *voltage-independent* phenomenon.

By recalling Figure 1, we note that R_c originates at multiple spots along the nanocomposite, therefore, we can only measure the net contribution of the multiple series-connected and parallel-connected constriction resistances, i.e., R_c forms an intricate network of resistances. The net contribution of the multiple constriction resistances, R_c , is henceforth designated as the contact resistance (R_{con}). We will no longer use R_c in this manuscript.

2.2.3. Combining Tunneling and Contact Resistances

Sensor resistance (R_{FSR}) is calculated by summing the contribution of the tunneling and the contact resistance as follows:

$$R_{FSR} = R_{tun} + R_{con} \quad (5)$$

Equation (5) was initially proposed by Kalantari et al. [45], and was later embraced by the authors [25].

As demonstrated in the next section, the random dispersion of conductive nanoparticles creates a specific sensor response in which either R_{tun} or R_{con} dominates for a given specimen. If particles are grouped in clusters separated by the insulating polymer, then R_{tun} dominates, but if particles are in direct contact (forming percolation paths), then R_{con} dominates. A discussion regarding the influence of U over R_{tun} and R_{con} can be found in previous works [25].

3. Materials and Methods

In previous work [55], the experimental setup was thoroughly described; therefore, only a brief description is presented here.

3.1. Mechanical Setup

The mechanical setup comprised a tailored test bench capable of handling up to 16 Interlink FSR402 sensors simultaneously; this let us speed up the characterization process by avoiding single-sensor measurement [55]. Forces were applied from a linear motor and a spring. An LCHD-5 load cell was deployed to close the force loop [30].

3.2. Electrical Setup

An amplifier in inverting configuration was used as the interface circuit; see Figure 2. This setup was preferably chosen over a voltage divider because the amplifier let us control the voltage across the sensor at any time. Analog multiplexers were deployed to enable time-multiplexed readings of the 16 FSRs. From the amplifier output voltage (U_o), we could determine sensor resistance, R_{FSR} , given the amplifier model:

$$U_o = -(R_f/R_{FSR}) \cdot U \quad (6)$$

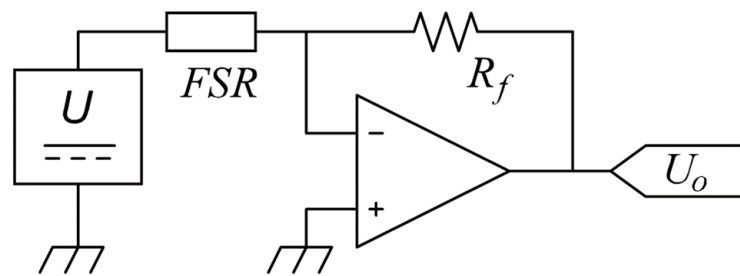


Figure 2. Electrical setup for driving the FSRs. The input voltage (U) was implemented from a digital-to-analog converter (DAC) to enable sensor characterization at multiple voltages.

From (6), we can either use R_{FSR} or U_o as the variable to measure. However, U_o was preferably chosen over R_{FSR} , because the former exhibited a linear relationship with the applied force, F . The feedback resistor (R_f) was set to 560Ω for all the experimental tests in this study. The acquisition system comprised a 16-bit analog-to-digital converter (ADC) model NI-9205 and a 16-bit digital-to-analog converter (DAC) model NI-9263; the former was required for measuring U_o , whereas the latter was employed to generate multiple U values. The system controller was the CRIO-9035 running LabVIEW Real Time.

3.3. Methods

Each step of the DMAIC cycle is briefly described in Table 1. A thorough description of the process is presented in the rest of the manuscript.

Table 1. Summary of the DMAIC cycle with a brief description of each step.

Step of the Cycle	Description
Define	Sensitivity (m) of 64 specimens of commercial FSRs, model Interlink FSR402 [27]. A total of 48 sensors were considered for the DMAI stages and 16 for the C stage.
Measure	Sensitivity was measured in force steps of 1 N, starting at 0 N up to 20 N. A total of 19 input voltages (U) were considered: 0.25 V, 0.5 V, 0.75 V, and 1 V. Above 1 V, voltage increments of 0.5 V were applied up to 8.5 V.
Analyze	Evaluation of the experimental data in perspective of the underlying physics of FSRs. Four claims were stated to ease the analysis and to derive conclusions.
Improve	The improve step comprised two stages: finding the optimal input voltage that minimizes dispersion in sensitivity, proposing and test two different methods to reduce the dispersion in sensitivity.
Control	Validate the two methods developed in the improve stage using 16 sensors.

Given the DMAIC cycle, we *defined* sensor sensitivity (m) as the variable to study with units of volts per Newton. The sensitivity *measurements* were performed at multiple input voltages as described in Table 1. From the 64 sensors at 19 different voltages, a total of 1216 sensitivities were collected. No lot control was considered for the 64 sensors; this is important to note because the manufacturer has stated different part-to-part repeatability for single-lot sensors [27]. Given the setup of Figure 2, sensitivity was obtained from a least-squares fitting process with general formula:

$$U_o = mF + b \quad (7)$$

where (b) was the y-intercept resulting from the fit. It must be clarified that b was not considered in this study; instead, we measured the output voltage at 0 N (U_o^{0N}). The reasoning behind this decision is provided in the next step. The *analysis* stage comprised an extensive evaluation of the experimental data in perspective of the theoretical foundations from Section 2. Before discussing the experimental data, we had to develop the following theoretical *claims*:

(i) Regardless of U , larger compressive forces increase the current density as the interparticle separation is reduced and the contact resistance is lowered; see (1)–(5). (ii) For null applied force, incremental U yields larger current density, thus U_o^{0N} is increased as well; see (2). However, we must recall that the constriction resistance is a voltage-independent phenomenon, thus changing U does not modify R_{con} ; see (4). (iii) By taking the derivative of $J(U,s(F))$ with respect to F , we note that for the same force profile, the derivative increases for larger U . The rate of change between $J(U,s(F))$ and F determines sensor sensitivity as it relates the change in sensor current with the input force; this statement only applies for the tunneling resistance. Claim (iii) can be summarized as follows: larger U yields greater sensitivity, whereas reducing U diminishes sensor sensitivity.

(iv) It is clear from Figure 1 that both piezoresistive phenomena occur simultaneously under any applied stress. Nonetheless, the experimental data support the hypothesis that one phenomenon usually dominates over the other for a given sensor. For example: when the contact resistance dominates, the percolation paths are the main source of piezoresistivity; whereas quantum tunneling is less important. Under this scenario, U_o^{0N} is large but m is small. To understand this, we must compare (2) and (3) with (4) as follows: given the predominant percolation paths along the FSR, a large U_o^{0N} is naturally expected because these paths tend to easily transport electrons from one electrode to the other, however, when an external force is applied, the change in resistance is small as predicted by (4), i.e., the contact resistance changes with the inverse of the applied force. In contrast, when quantum tunneling dominates, the percolation paths are incomplete or nonexistent; in this case, (2) and (3) instead play a major role. Under this scenario, a small increment in s —caused by an external force—results in a dramatic change in current density due to the exponential dependence in (2) and (3); this can be understood as a large sensitivity. Nonetheless, when quantum tunneling dominates and the sensor is unloaded, U_o^{0N} is small because there are not percolation paths that connect both electrodes.

Experimental results supporting previous statements are next presented. Thereafter, *improve* and *control* stages are described.

4. Results

Figure 3 shows the experimental data for two specimens at different input voltages. The claims (i)–(iv) from Section 3 can be validated with the results reported in this figure, as follows: (i) larger forces increase U_o ; (ii) for a given sensor, increasing U , also increases U_o^{0N} , and similarly, (iii) larger U increases m as well. Finally, (iv) if U_o^{0N} is large, then percolation dominates and m is usually small. The opposite case can be also observed in Figure 3; if U_o^{0N} is small, then quantum tunneling dominates, and m is generally large.

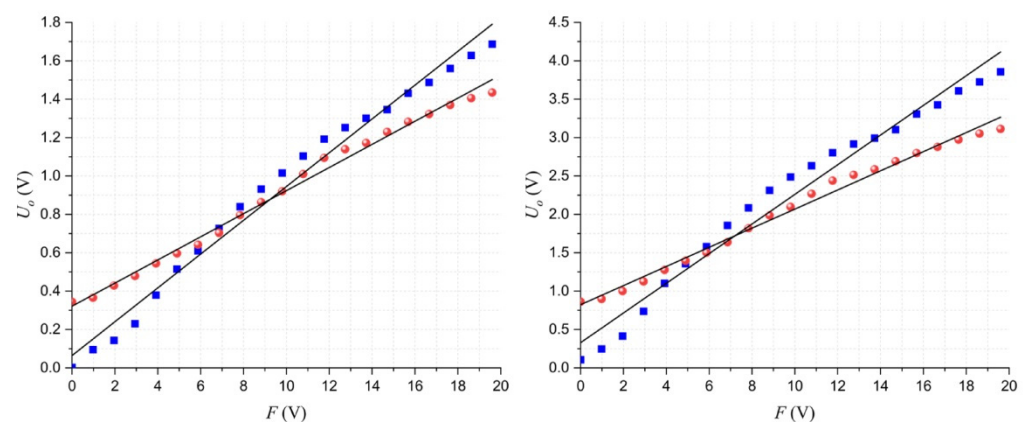


Figure 3. Plots of the output voltage (U_o) as a function of the applied force (F) for two different specimens at different input voltages (U). The fit to (7) has been overlaid in both cases. The sensor where percolation dominates is shown with red spherical markers; the sensor where quantum tunneling dominates is shown with blue square markers. Data taken at (left) $U = 3$ V and (right) $U = 6$ V.

From the experimental data resulting at each input voltage, we obtained sensor sensitivity for each specimen; then, we calculated the mean (μ) and standard deviation, σ , at each U using a probability fit to a Gaussian distribution. Previously, we applied Anderson-Darling tests to verify the null hypothesis to different probability distributions; the Gaussian distribution was the most likely distribution for each dataset.

As a part of the *improve* stage, the ratio of μ/σ as a function of U is shown in Figure 4; this chart lets us assess which input voltage naturally yields the highest part-to-part repeatability. The quotient μ/σ is known in literature as the inverse of the coefficient of variation. Note that at $U = 3$ V, the dispersion in sensitivity is the lowest. Hence, we can state that when operating Interlink sensors at 3 V, part-to-part repeatability is naturally maximized. We focus on this start point to further reduce σ . As previously mentioned, this study comprised the application of compensation techniques at the last stage of final application deployment, therefore, we could only trim U to target a desired sensitivity for a given sensor; see claim (iii) from the *Methods* section. In practice, it was possible to change U by means of a DAC; see Figure 2.

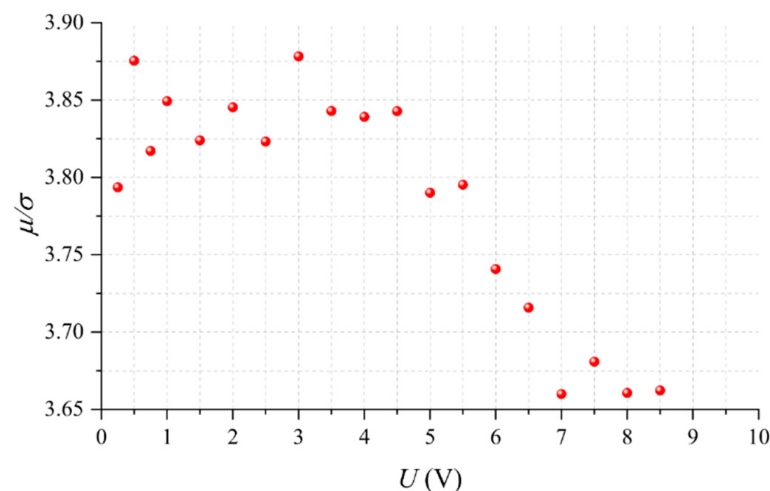


Figure 4. Inverse of the coefficient of variation (μ/σ) estimated at different input voltages (U) for the 48 sensors under study. Probability fitting to a Gaussian distribution was performed at each U to estimate μ and σ .

4.1. Sensor Classification on the Basis of the Output Voltage at Null Force

From the experimental data taken at $U = 3$ V, we plotted in Figure 5 each sensor sensitivity, m , with its corresponding output voltage at null force, U_o^{0N} . Later, the experimental data were fitted to a Gaussian probability distribution resulting in a mean value of $\mu_{3V} = 0.0735$ V/N with standard deviation $\sigma_{3V} = 0.019$ V/N.

As predicted by claim (iv), we observed that sensors exhibiting a large U_o^{0N} tend to show a low m , and that similarly, sensors with a small U_o^{0N} tended to show a large m . In other words, U_o^{0N} is approximately related to sensor sensitivity. To the best of the authors' knowledge, this observation has not been published elsewhere in specialized literature, but it represents a powerful tool, as described in the next paragraph. For compensation purposes in the *improve* stage, we have segmented the dataset from Figure 5 into three regions according to U_o^{0N} : (A) sensors where quantum tunneling dominates that meet the criteria $U_o^{0N} < U_{th}^{low}$, (B) sensors where quantum tunneling and contact resistance have similar weight, and (C), sensors where contact resistance dominates that meet the criteria $U_o^{0N} > U_{th}^{high}$. The procedure for setting the threshold voltages (U_{th}^{low} , U_{th}^{high}) is described in the next section.

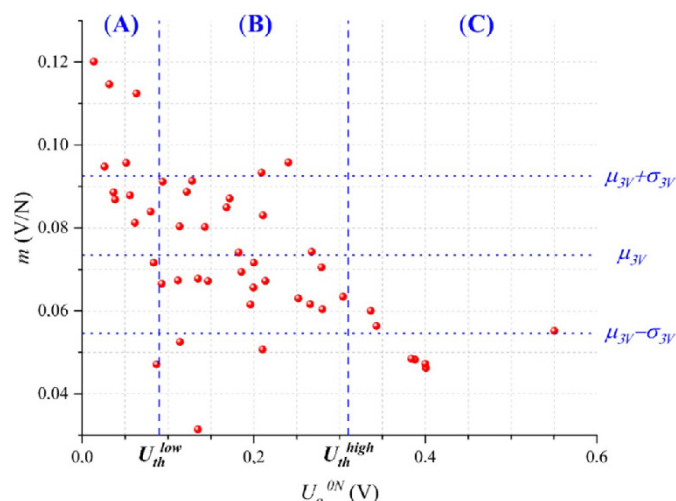


Figure 5. Sensitivity (m) as a function of the output voltage at null force (U_o^{0N}) for each specimen. The sensitivity data were fit to a Gaussian probability distribution resulting in the mean, $\mu_{3V} = 0.0735$ V/N, and standard deviation, $\sigma_{3V} = 0.019$ V/N. Low threshold voltage (U_{th}^{low}) and high threshold voltage (U_{th}^{high}) were defined for classification purposes. Data were taken at $U = 3$ V for 48 sensors.

The Importance of U_o^{0N} for assessing sensor’s sensitivity is twofold. First, U_o^{0N} can be measured at negligible cost after product manufacturing, i.e., a simple driving circuit is required with no mechanical setup, see Figure 2. Second, we can discard non-compliant sensors based on U_o^{0N} measurements; this ultimately enhances part-to-part repeatability as described next: by keeping the sensors that meet the criteria $U_{th}^{high} < U_o^{0N} < U_{th}^{low}$, we retain the sensors from Region (B) and discard the sensors from Regions (A) and (C). In practice, this implies that 19 out of the 48 sensors are discarded and 29 are kept; it must be emphasized that the sensors from Region (B) represent our desired target, for this reason, we discard the noncompliant sensors belonging to Regions (A) and (C).

Subsequently, we perform a new fit to a Gaussian distribution from the 29 selected sensors that results in the mean $\mu_B = 0.0718$ V/N with standard deviation $\sigma_B = 0.0142$ V/N. Note that μ_B slightly changed from the previously reported value of $\mu_{3V} = 0.0735$ V/N, but that σ_B decreased 25% from its original value of $\sigma_{3V} = 0.019$ V/N. From a Six Sigma standpoint, this represents a 1.5σ improvement. Finally, the quotient μ_B/σ_B can be recalculated with the 29 selected sensors as 5.05, which is greater than the value of 3.87 reported in Figure 4. This simple procedure is useful for enhancing part-to-part repeatability, but unfortunately, it occurs at the cost of discarding sensors, which unavoidably represents material waste. Therefore, in the next section, we introduce an alternative compensation technique for the sensors in Regions (A) and (C).

Before proceeding with the compensation technique, we must recall the random distribution of nanoparticles along the polymer matrix. This fact unavoidably causes some specimens from Region (B) to show either a sensitivity larger than $\mu_{3V} + \sigma_{3V}$ or lower than $\mu_{3V} - \sigma_{3V}$; the physical reasons for this behavior are manifold, but we can point out some of them: a given specimen may have a particle count below average; thus, sensitivity is lowered. Another possible reason is the random spacing of clusters that creates isolated conglomerates in the polymer matrix; these separated clusters are just too far from each other to enable quantum tunneling. See Figure 1 for a schematic representation of this.

4.2. Compensation Technique to Enhance Part-to-Part Repeatability

Following the *improve* stage; new driving voltages must be found for the sensors belonging to Regions (A) and (C), see Figure 5; this procedure is supported by claim (iii). By doing this, we can closely match each specimen’s sensitivity with μ_{3V} , i.e., the target sensitivity.

For the sensors belonging to Region (A), we must find a new U that lowers the sensitivity of each specimen. In this case, the new U must be lower than 3 V. For the sensors belonging to Region (C), the opposite occurs; the new input voltage must be higher than 3 V to increase their sensitivity. As stated in claim (ii), a change in U also modifies U_o^{0N} ; this is not a problem itself because U_o^{0N} can be measured anytime in the final application.

In order to find a relationship among m , U_o^{0N} , and U , we plotted them together in Figure 6 for the sensors belonging to Region (A). Then, a least-squares fit was applied to find a numerical expression that relates these three variables. The best, yet simplest, function was found to be:

$$U = a \cdot \hat{U}_o^{0N} + b \cdot \hat{m} + c \tag{8}$$

where a, b, c are coefficients resulting from the fit. Normalization was performed for the variables U_o^{0N} and m , where $\hat{U}_o^{0N} = U_o^{0N} / U$ and $\hat{m} = m / U$. By doing this, we avoided quadratic functions and used a simple 3D plane resulted instead. The same procedure was repeated for the sensors belonging to Region (C). Both fitting results are summarized in Table 2. The fit to (8) allowed us to determine the optimal threshold voltages for regions (A), (B), and (C). The threshold voltages, U_{th}^{low} and U_{th}^{high} , were previously defined in Figure 5; they let us assess whether quantum tunneling or constriction resistance dominates for a given sensor. The procedure for determining U_{th}^{low} and U_{th}^{high} is described next.

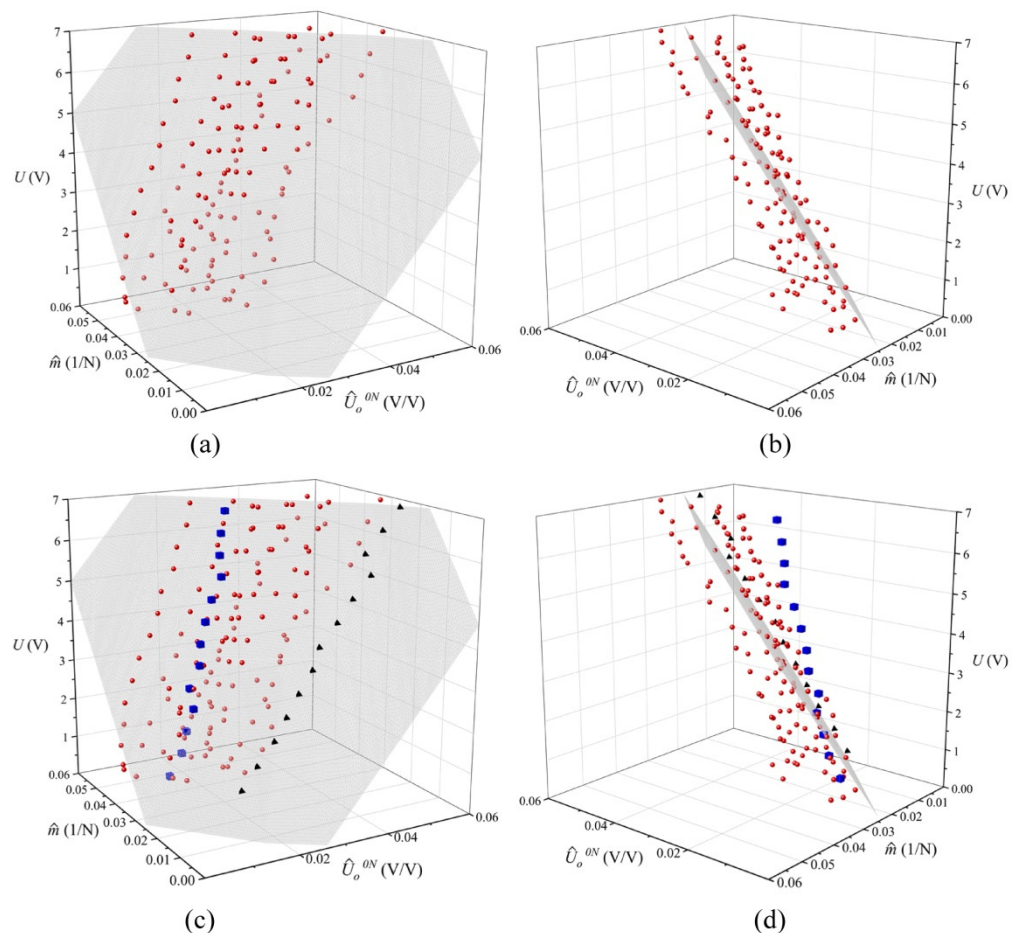


Figure 6. 3D plot of the normalized sensitivity (\hat{m}), the normalized output voltage at null force (\hat{U}_o^{0N}), and the input voltage (U). Data corresponding to the 12 sensors belonging to Region (A). (a,b) Isometric views of the 3D fit using Equation (8) as the model with parameters shown in Table 2. (c,d) Isometric views of the 3D fit with special markers. The blue cubes and black pyramid markers correspond to individual sensors that shift in different directions along the plane when U is changed.

Table 2. Parameters resulting from the fit. Parameters a through c were obtained from a least-squares fit to (8) with coefficient of correlation R^2 . The mean sensitivity (μ) for each region (μ_A , μ_C) was measured at $U = 3$ V.

	a (V)	b (N·V)	c (V)	R^2	μ (V/N)
Region (A)	132.3	139.1	−3.36	0.67	$\mu_A = 0.091$
Region (C)	101	485.2	−18.2	0.94	$\mu_C = 0.052$

The higher U_{th}^{low} is set, the more sensors are considered as a part of Region (A). However, by doing this, the coefficient of determination (R^2) resulting from the fit is reduced; this occurs because we are embracing sensors that fall out the criteria for this region, i.e., in Region (A) quantum tunneling dominates. The same procedure was repeated to obtain U_{th}^{high} , but in this case, U_{th}^{high} has to be reduced in order to embrace more sensors in Region (C). In practice, U_{th}^{low} and U_{th}^{high} were found by an iterative process that aimed to obtain the largest U_{th}^{low} that minimized R^2 in Region (A), and the smallest U_{th}^{high} that minimized R^2 in Region (C). Finally, U_{th}^{low} and U_{th}^{high} resulted in 90 mV and 310 mV, respectively.

Compensating voltages for the sensors in Region (A) and (C) can also be found from (8). Nonetheless, we cannot directly replace U_o^{0N} in (8) and set a targeted sensitivity, m , to obtain the new U . As previously mentioned, a change in U modifies both: U_o^{0N} and m ; see claims (ii), (iii). The 3D surface resulting from (8) can be understood as the plane where U_o^{0N} and m are shifted when U is changed. Nonetheless, every sensor exhibits a different rate of change in U_o^{0N} as a function of U ; this is exemplified with the pyramid and cubic markers in Figure 6. Each marker corresponds to individual sensor data that can be well fitted in the 3D plane, but they move in different angles along the surface when U is changed. Therefore, we are limited to obtain an average rate of change for U_o^{0N} as a function of U ; this average comprises the 12 sensors belonging to Region (A). In the Conclusion section, the scenario is discussed when we consider an individual rate of change for each sensor.

Finally, given the mean sensitivity at 3 V for the sensors in Region (A), μ_A , the model from (8), the target sensitivity, μ_{3V} , and the average rate of change of U_o^{0N} as a function of U , we computed the new U resulting in $U_A = 2.5$ V. Similarly, the same procedure was performed for the sensors in Region (C), but using μ_C and the average rate of change of U_o^{0N} for these sensors; this resulted in the new voltage of $U_C = 3.15$ V.

Later, experimental sensor characterization was performed at the new voltages U_A and U_C ; this was done for the sensors belonging to Regions (A) and (C), respectively. The experimental results are plotted in Figure 7. Nonetheless, the sensor data from Region (B) is the same plotted in Figure 5 since U remained unchanged for these sensors. For the whole dataset for Figure 7, a new fit to a Gaussian distribution was performed, resulting in $\mu_{comp} = 0.0727$ V/N and $\sigma_{comp} = 0.016$ V/N. This represents a 15% reduction in the standard deviation when compared with σ_{3V} . Although this reduction in the standard deviation is lower than previously reported for the discarding method; it is demonstrated that changing U is an effective way to fine-tune the sensitivity of FSRs.

4.3. Assessing the Compensation Technique from a Six Sigma Perspective

As a part of the *control* stage of the DMAIC cycle, we tested an additional group of 16 Interlink FSR 402 sensors. These sensors were initially characterized at $U = 3$ V to obtain U_o^{0N} and m . Figure 8 shows the summary of this characterization with an overlay of U_{th}^{low} , U_{th}^{high} , μ_{3V} , and σ_{3V} for classification purposes. An Anderson-Darling test to different probability distributions demonstrated that these data could be well fitted to a Gaussian distribution with $\mu_{control} = 0.0774$ V/N and $\sigma_{control} = 0.0189$ V/N. Note that the start point before compensation was quite similar to μ_{3V} and σ_{3V} from the *improve* stage.

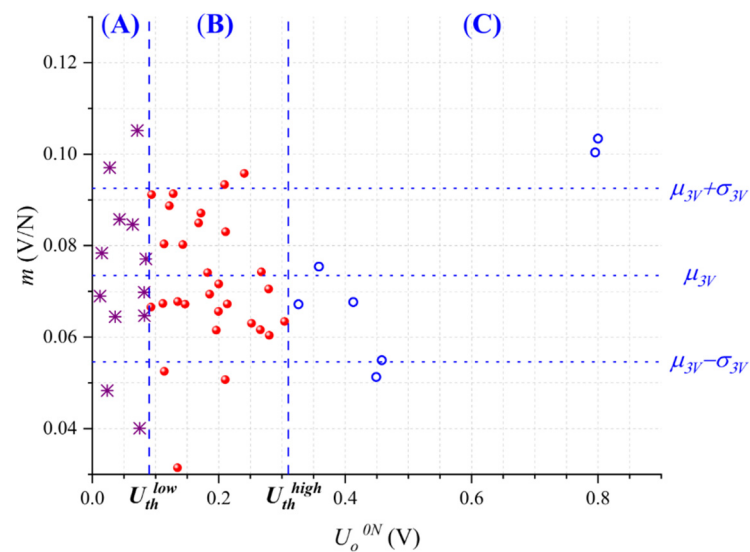


Figure 7. Sensitivity (m) as a function of the output voltage at null force (U_o^{0N}) for each specimen after compensation. Compensation was performed for the sensors belonging to Regions (A) and (C) using different input voltages (U_A, U_C). For comparison purposes, the y-axis scale was held unchanged from Figure 5. Different markers were used for the sensors of Regions (A) and (C) after compensation.

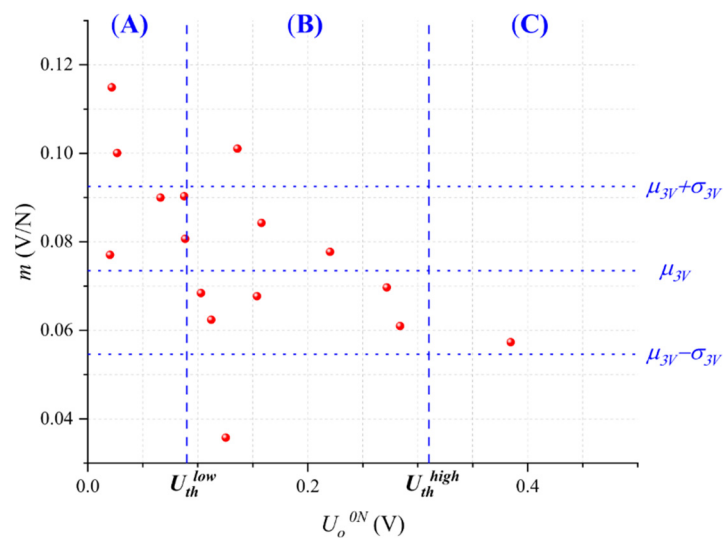


Figure 8. Sensitivity (m) as a function of the output voltage at null force (U_o^{0N}) for the sixteen specimens of the *control* stage. Data were taken at $U = 3$ V.

Later, we classified the sensors belonging to Regions (A), (B), and (C) on the basis of U_{th}^{low} and U_{th}^{high} . Part-to-part repeatability was enhanced following two different approaches: first, by discarding the sensors from Regions (A) and (C) and keeping only those from Region (B), and second, by applying the compensation technique based on changing U .

From the first approach, 7 out of the 16 sensors were discarded and 9 were kept. Then, we recalculated the mean and standard deviation, obtaining 0.0698 V/N and 0.0168 V/N, respectively; this represents an 11% reduction in the standard deviation and a Six Sigma improvement of 0.66σ . However, note that the mean sensitivity was altered from its original value.

From the second approach, new characterization was performed at the input voltages U_A and U_C for the sensors belonging to Regions (A) and (C), respectively. No compensation was performed for the sensors belonging to Region (B). The experimental results are shown

in Figure 9. Later, we recalculated the mean and standard deviation, obtaining 0.0726 V/N and 0.0154 V/N, respectively; this represents an 18.5% reduction in the standard deviation amid a negligible variation for the mean sensitivity. This represents a 1.1σ improvement using the Six Sigma approach.

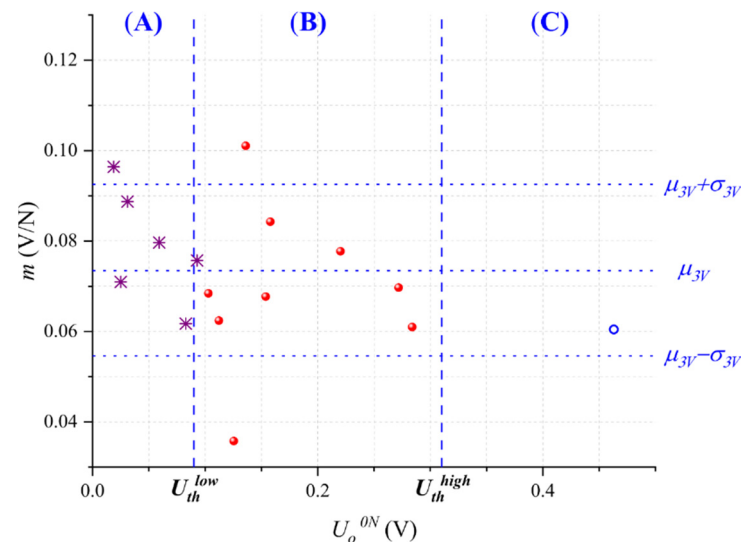


Figure 9. Sensitivity (m) as a function of the output voltage at null force (U_o^{0N}) for each specimen after compensation. Experimental data resulting from the *control* stage. Different markers were used for the sensors of Regions (A) and (C) after compensation.

4.4. Practical Considerations for the Implementation of the Proposed Methods

First of all, it must be emphasized that this research did not consider lot control for the specimens characterized. Therefore, if the manufacturing conditions remain unchanged over time (e.g., particle dimension, type of polymer, preparation conditions, and so on), the compensation techniques should work for any specimen of Interlink FSR 402. In regard to the feedback resistor, a change in R_f produces a linear variation in the magnitude of m , U_o^{0N} , U_{th}^{low} and U_{th}^{high} ; this occurs because the amplifier is an inherently linear device. Therefore, if R_f is doubled or halved, the aforementioned magnitudes also change proportionally.

Nonetheless, a change in the driving voltage would impact m , U_o^{0N} , U_{th}^{low} , and U_{th}^{high} in a nonlinear fashion; this is expected because quantum tunneling is a nonlinear phenomenon. Besides, we must recall that during the *improve* stage, we found $U = 3$ V as the optimal voltage that naturally maximizes the quotient μ/σ ; see Figure 4. Therefore, we set $U = 3$ V as the starting point to subsequently trim the input voltage in the *improve* and *control* stages. However, if we set a different starting point for U , we would deviate from the results reported here.

Finally, given the relatively low number of sensors considered in this research (64 specimens), only three regions were defined. By considering more regions, a more suitable compensating voltage could be applied for each specimen. The experimental data employed in this study can be found in [56].

5. Conclusions

Changing the input voltage is an effective way to trim the sensitivity of force-sensing resistors (FSRs). The output voltage at null force (U_o^{0N}) can give us a hint about the individual sensor's sensitivity without requiring individual characterization. To the best of authors' knowledge, this observation has not been reported elsewhere. With the information provided from U_o^{0N} , we could set new input voltages that let us reduce the dispersion in sensors' sensitivity and/or discard noncompliant sensors. Both methods were explored in this study, resulting in a reduction of 18.5% and 11% in the standard deviation of sensor sensitivity for each procedure, respectively. These results were obtained in the *control*

stage of the DMAIC cycle for a bunch of 16 Interlink FSR 402 sensors. These percentages represent 1.1σ and 0.66σ improvements according to the Six Sigma methodology.

A promising technique to be explored in the authors' future work is based on individually defining new input voltages for each sensor; by doing this, we can more accurately match the sensitivity of each specimen with a target sensitivity, thus achieving a larger Six Sigma improvement. However, this procedure requires that we previously track U_o^{ON} for multiple input voltages and later incorporate such information in the final compensation formula.

Author Contributions: Conceptualization, L.P.-M. and A.O.G.-P.; hardware set-up, A.P.; figure design and data analysis, V.M.F.; validation, C.P. All authors have read and agreed to the published version of the manuscript.

Funding: This work was funded by Universidad Católica de Colombia through the Internal Call for Projects 2021, grant No CON0000456 and by Universidad Antonio Nariño through grant No PI/UAN-2021-701GIBIO.

Data Availability Statement: Experimental data can be found here [56].

Conflicts of Interest: The authors declare no conflict of interest.

Appendix A. Foundations of the Six Sigma Methodology

Six Sigma is a continuous improvement methodology that has been widely applied in the manufacturing and services sectors. Its implementation focuses on the application of the DMAIC cycle (Define, Measure, Analyze, Improve, and Control) [41]. This methodology is based on the reduction of the process variability regarding a Critical to Quality (CTQ) or critical variable for the process or the client. Process variability is assessed on the basis of the standard deviation (σ) for any process parameter, e.g., when building antennas on a printed circuit board (PCB), the width and length of the paths have a strong influence on the antennas' bandwidth and frequency response [57]; therefore, we can deploy the DMAIC cycle to reduce the dispersion of the width and length of paths from their nominal value.

Six Sigma requires the collection of data and the application of analytical and statistical tools to identify the causes of the variation and thus achieve a 6σ level that translates into 3.4 errors per million opportunities [41]. A 6σ level implies that standard deviation is reduced by a factor of 6 from the original assessment. The opportunity is understood as the probability of noncompliance or the probability of not meeting the required specifications. The DMAIC cycle implemented by the Six Sigma methodology is used to identify and solve problems related to the process; analyzing the current state of a problem of interest, find its root cause, propose improvement solutions, and keep them durable over time.

References

1. Yeasmin, R.; Duy, L.T.; Han, S.; Seo, H. Intrinsically Stretchable and Self-Healing Electroconductive Composites Based on Supramolecular Organic Polymer Embedded with Copper Microparticles. *Adv. Electron. Mater.* **2020**, *6*, 2000527. [[CrossRef](#)]
2. Wang, X.; Liu, X.; Schubert, D.W. Highly Sensitive Ultrathin Flexible Thermoplastic Polyurethane/Carbon Black Fibrous Film Strain Sensor with Adjustable Scaffold Networks. *Nano-Micro Lett.* **2021**, *13*, 64. [[CrossRef](#)] [[PubMed](#)]
3. Yang, H.; Yuan, L.; Yao, X.; Zheng, Z.; Fang, D. Monotonic Strain Sensing Behavior of Self-Assembled Carbon Nanotubes/Graphene Silicone Rubber Composites under Cyclic Loading. *Compos. Sci. Technol.* **2020**, *200*, 108474. [[CrossRef](#)]
4. Zhao, Y.; Ren, M.; Shang, Y.; Li, J.; Wang, S.; Zhai, W.; Zheng, G.; Dai, K.; Liu, C.; Shen, C. Ultra-Sensitive and Durable Strain Sensor with Sandwich Structure and Excellent Anti-Interference Ability for Wearable Electronic Skins. *Compos. Sci. Technol.* **2020**, *200*, 108448. [[CrossRef](#)]
5. Xiang, D.; Zhang, X.; Han, Z.; Zhang, Z.; Zhou, Z.; Harkin-Jones, E.; Zhang, J.; Luo, X.; Wang, P.; Zhao, C.; et al. 3D Printed High-Performance Flexible Strain Sensors Based on Carbon Nanotube and Graphene Nanoplatelet Filled Polymer Composites. *J. Mater. Sci.* **2020**, *55*, 15769–15786. [[CrossRef](#)]
6. Fekiri, C.; Kim, H.C.; Lee, I.H. 3d-Printable Carbon Nanotubes-Based Composite for Flexible Piezoresistive Sensors. *Materials* **2020**, *13*, 5482. [[CrossRef](#)]
7. Aikawa, S.; Zhao, Y.; Yan, J. Development of High-Sensitivity Electrically Conductive Composite Elements by Press Molding of Polymer and Carbon Nanofibers. *Micromachines* **2022**, *13*, 170. [[CrossRef](#)]

8. Li, F.-C.; Kong, Z.; Wu, J.-H.; Ji, X.-Y.; Liang, J.-J. Advances in Flexible Piezoresistive Pressure Sensor. *Wuli Xuebao Acta Phys. Sin.* **2021**, *70*, 100703. [CrossRef]
9. Kanoun, O.; Bouhamed, A.; Ramalingame, R.; Bautista-Quijano, J.R.; Rajendran, D.; Al-Hamry, A. Review on Conductive Polymer/CNTs Nanocomposites Based Flexible and Stretchable Strain and Pressure Sensors. *Sensors* **2021**, *21*, 341. [CrossRef]
10. Kim, K.; Shin, S.; Kong, K. An Air-Filled Pad With Elastomeric Pillar Array Designed for a Force-Sensing Insole. *IEEE Sens. J.* **2018**, *18*, 3968–3976. [CrossRef]
11. Chen, D.; Cai, Y.; Huang, M.-C. Customizable Pressure Sensor Array: Design and Evaluation. *IEEE Sens. J.* **2018**, *18*, 6337–6344. [CrossRef]
12. Aoyagi, S.; Suzuki, M.; Morita, T.; Takahashi, T.; Takise, H. Bellows Suction Cup Equipped With Force Sensing Ability by Direct Coating Thin-Film Resistor for Vacuum Type Robotic Hand. *IEEEASME Trans. Mechatron.* **2020**, *25*, 2501–2512. [CrossRef]
13. Liang, J.; Wu, J.; Huang, H.; Xu, W.; Li, B.; Xi, F. Soft Sensitive Skin for Safety Control of a Nursing Robot Using Proximity and Tactile Sensors. *IEEE Sens. J.* **2020**, *20*, 3822–3830. [CrossRef]
14. Zhang, H.; Ren, P.; Yang, F.; Chen, J.; Wang, C.; Zhou, Y.; Fu, J. Biomimetic Epidermal Sensors Assembled from Polydopamine-Modified Reduced Graphene Oxide/Polyvinyl Alcohol Hydrogels for the Real-Time Monitoring of Human Motions. *J. Mater. Chem. B* **2020**, *8*, 10549–10558. [CrossRef]
15. Sun, X.; Liu, T.; Zhou, J.; Yao, L.; Liang, S.; Zhao, M.; Liu, C.; Xue, N. Recent Applications of Different Microstructure Designs in High Performance Tactile Sensors: A Review. *IEEE Sens. J.* **2021**, *21*, 10291–10303. [CrossRef]
16. Boada, M.; Lazaro, A.; Villarino, R.; Gil, E.; Girbau, D. Battery-Less NFC Bicycle Tire Pressure Sensor Based on a Force-Sensing Resistor. *IEEE Access* **2021**, *9*, 103975–103987. [CrossRef]
17. Pang, G.; Deng, J.; Wang, F.; Zhang, J.; Pang, Z.; Yang, G. Development of Flexible Robot Skin for Safe and Natural Human–Robot Collaboration. *Micromachines* **2018**, *9*, 576. [CrossRef]
18. Cavallo, A.; Beccatelli, M.; Favero, A.; Al Kayal, T.; Seletti, D.; Losi, P.; Soldani, G.; Coppedè, N. A Biocompatible Pressure Sensor Based on a 3D-Printed Scaffold Functionalized with PEDOT:PSS for Biomedical Applications. *Org. Electron.* **2021**, *96*, 106204. [CrossRef]
19. Fernandez, F.D.M.; Khadka, R.; Yim, J.-H. Highly Porous, Soft, and Flexible Vapor-Phase Polymerized Polypyrrole-Styrene-Ethylene-Butylene-Styrene Hybrid Scaffold as Ammonia and Strain Sensor. *RSC Adv.* **2020**, *10*, 22533–22541. [CrossRef]
20. Lo, L.-W.; Zhao, J.; Wan, H.; Wang, Y.; Chakraborty, S.; Wang, C. An Inkjet-Printed PEDOT:PSS-Based Stretchable Conductor for Wearable Health Monitoring Device Applications. *ACS Appl. Mater. Interfaces* **2021**, *13*, 21693–21702. [CrossRef]
21. Ou, L.; Song, B.; Liang, H.; Liu, J.; Feng, X.; Deng, B.; Sun, T.; Shao, L. Toxicity of Graphene-Family Nanoparticles: A General Review of the Origins and Mechanisms. *Part. Fibre Toxicol.* **2016**, *13*, 57. [CrossRef] [PubMed]
22. Zhang, K.; Song, C.; Wang, Z.; Gao, C.; Wu, Y.; Liu, Y. A Stretchable and Self-Healable Organosilicon Conductive Nanocomposite for a Reliable and Sensitive Strain Sensor. *J. Mater. Chem. C* **2020**, *8*, 17277–17288. [CrossRef]
23. Hussain, I.; Ma, X.; Luo, Y.; Luo, Z. Fabrication and Characterization of Glycogen-Based Elastic, Self-Healable, and Conductive Hydrogels as a Wearable Strain-Sensor for Flexible e-Skin. *Polymer* **2020**, *210*, 122961. [CrossRef]
24. Ma, Z.; Li, H.; Jing, X.; Liu, Y.; Mi, H.-Y. Recent Advancements in Self-Healing Composite Elastomers for Flexible Strain Sensors: Materials, Healing Systems, and Features. *Sens. Actuators Phys.* **2021**, *329*, 112800. [CrossRef]
25. Paredes-Madrid, L.; Palacio, C.A.; Matute, A.; Parra Vargas, C.A. Underlying Physics of Conductive Polymer Composites and Force Sensing Resistors (FSRs) under Static Loading Conditions. *Sensors* **2017**, *17*, 2108. [CrossRef]
26. Paredes-Madrid, L.; Fonseca, J.; Matute, A.; Gutiérrez Velásquez, E.I.; Palacio, C.A. Self-Compensated Driving Circuit for Reducing Drift and Hysteresis in Force Sensing Resistors. *Electronics* **2018**, *7*, 146. [CrossRef]
27. Interlink Electronics FSR400 Series Datasheet. 2017. Available online: <https://f.hubspotusercontent20.net/hubfs/3899023/Integration%20Guides/FSR%20X%20%26%20UX%20Integration%20Guide%20-%20Interlink%20Electronics.pdf> (accessed on 26 April 2022).
28. Peratech Inc. QTC SP200 Series Datasheet. Single Point Sensors. 2015. Available online: <https://www.peratech.com/assets/uploads/datasheets/Peratech-QTC-DataSheet-SP200-Series-Nov15.pdf> (accessed on 26 April 2022).
29. Tekscan Inc. FlexiForce, Standard Force & Load Sensors Model A201. Datasheet. 2017. Available online: <https://www.tekscan.com/sites/default/files/resources/FLX-Datasheet-A201-RevI.pdf> (accessed on 26 April 2022).
30. Omega Ultra Low Profile, Tension and Compression Load Cells. 2021. Available online: <https://www.omega.com/en-us/force-strain-measurement/load-cells/lchd/p/LCHD-7-5K> (accessed on 26 April 2022).
31. Urban, S.; Ludersdorfer, M.; van der Smagt, P. Sensor Calibration and Hysteresis Compensation with Heteroscedastic Gaussian Processes. *IEEE Sens. J.* **2015**, *15*, 6498–6506. [CrossRef]
32. Nguyen, X.A.; Chauhan, S. Characterization of Flexible and Stretchable Sensors Using Neural Networks. *Meas. Sci. Technol.* **2021**, *32*, 075004. [CrossRef]
33. Albright, T.B.; Hobeck, J.D. High-Fidelity Stochastic Modeling of Carbon Black-Based Conductive Polymer Composites for Strain and Fatigue Sensing. *J. Mater. Sci.* **2021**, *56*, 6861–6877. [CrossRef]
34. Castellanos-Ramos, J.; Navas-Gonzalez, R.; Macior, H.; Sikora, T.; Ochoteco, E.; Vidal-Verdu, F. Tactile Sensors Based on Conductive Polymers. *Microsys. Technol.* **2010**, *16*, 765–776. [CrossRef]
35. Meyer, D.; Maehling, P.; Varghese, T.; Lewis, J. Calibration Considerations for Six SigmaTM Accuracy and Precision in Combustion Pressure Measurement. *SAE Int. J. Commer. Veh.* **2017**, *10*, 508–517. [CrossRef]

36. Milačič, M.; Booden, V.; Grimes, J.; Maier, B. Hydrogen Leak Detection Method Derived Using DCOV Methodology. *SAE Tech. Pap.* **2009**, *9*, 97–102. [[CrossRef](#)]
37. Yusof, N.S.B.; Sapuan, S.M.; Sultan, M.T.H.; Jawaid, M. Materials Selection of “Green” Natural Fibers in Polymer Composite Automotive Crash Box Using DMAIC Approach in Six Sigma Method. *J. Eng. Fibers Fabr.* **2020**, *15*, 1558925020920773. [[CrossRef](#)]
38. Prabhakaran, R.T.D.; Babu, B.J.C.; Agrawal, V.P. Quality Modeling and Analysis of Polymer Composite Products. *Polym. Compos.* **2006**, *27*, 329–340. [[CrossRef](#)]
39. Arvidsson, M.; Gremyr, I.; Johansson, P. Use and Knowledge of Robust Design Methodology: A Survey of Swedish Industry. *J. Eng. Des.* **2003**, *14*, 129–143. [[CrossRef](#)]
40. Lucero, B.; Linsey, J.; Turner, C.J. Frameworks for Organising Design Performance Metrics. *J. Eng. Des.* **2016**, *27*, 175–204. [[CrossRef](#)]
41. Pyzdek, T. *The Six Sigma Handbook, Revised and Expanded*; McGraw Hill: New York, NY, USA, 2002.
42. Dauzon, E.; Lin, Y.; Faber, H.; Yengel, E.; Sallenave, X.; Plesse, C.; Goubard, F.; Amassian, A.; Anthopoulos, T.D. Stretchable and Transparent Conductive PEDOT:PSS-Based Electrodes for Organic Photovoltaics and Strain Sensors Applications. *Adv. Funct. Mater.* **2020**, *30*, 2001251. [[CrossRef](#)]
43. Cvek, M.; Kutalkova, E.; Moucka, R.; Urbanek, P.; Sedlacik, M. Lightweight, Transparent Piezoresistive Sensors Conceptualized as Anisotropic Magneto-rheological Elastomers: A Durability Study. *Int. J. Mech. Sci.* **2020**, *183*, 105816. [[CrossRef](#)]
44. Ding, S.; Han, B.; Dong, X.; Yu, X.; Ni, Y.; Zheng, Q.; Ou, J. Pressure-Sensitive Behaviors, Mechanisms and Model of Field Assisted Quantum Tunneling Composites. *Polymer* **2017**, *113*, 105–118. [[CrossRef](#)]
45. Kalantari, M.; Dargahi, J.; Kovacs, J.; Mardasi, M.G.; Nouri, S. A New Approach for Modeling Piezoresistive Force Sensors Based on Semiconductive Polymer Composites. *IEEE ASME Trans. Mechatr.* **2012**, *17*, 572–581. [[CrossRef](#)]
46. Li, C.; Thostenson, E.T.; Chou, T.-W. Dominant Role of Tunneling Resistance in the Electrical Conductivity of Carbon Nanotube-Based Composites. *Appl. Phys. Lett.* **2007**, *91*, 223114. [[CrossRef](#)]
47. Awasthi, S.; Gopinathan, P.S.; Rajanikanth, A.; Bansal, C. Current–Voltage Characteristics of Electrochemically Synthesized Multi-Layer Graphene with Polyaniline. *J. Sci. Adv. Mater. Dev.* **2018**, *3*, 37–43. [[CrossRef](#)]
48. Oskouyi, A.B.; Uttandaraman, S.; Mertiny, P. Current-Voltage Characteristics of Nanoplatelet-Based Conductive Nanocomposites. *Nanoscale Res. Lett.* **2014**, *9*, 369. [[CrossRef](#)] [[PubMed](#)]
49. Panozzo, F.; Zappalorto, M.; Quaresimin, M. Analytical Model for the Prediction of the Piezoresistive Behavior of {CNT} Modified Polymers. *Compos. Part B Eng.* **2017**, *109*, 53–63. [[CrossRef](#)]
50. Clayton, M.F.; Bilodeau, R.A.; Bowden, A.E.; Fullwood, D.T. Nanoparticle Orientation Distribution Analysis and Design for Polymeric Piezoresistive Sensors. *Sens. Actuators Phys.* **2020**, *303*, 111851. [[CrossRef](#)]
51. Simmons, J. Electrical Tunnel Effect between Dissimilar Electrodes Separated by a Thin Insulating Film. *J. Appl. Phys.* **1963**, *34*, 2581–2590. [[CrossRef](#)]
52. Zhang, X.-W.; Pan, Y.; Zheng, Q.; Yi, X.-S. Time Dependence of Piezoresistance for the Conductor-Filled Polymer Composites. *J. Pol. Sci. Part B Pol. Phys.* **2000**, *38*, 2739–2749. [[CrossRef](#)]
53. Esquinazi, P.; Barzola-Quiquia, J.; Dusari, S.; García, N. Length Dependence of the Resistance in Graphite: Influence of Ballistic Transport. *J. Appl. Phys.* **2012**, *111*, 033709. [[CrossRef](#)]
54. Mikrajuddin, A.; Shi, F.G.; Kim, H.K.; Okuyama, K. Size-Dependent Electrical Constriction Resistance for Contacts of Arbitrary Size: From Sharvin to Holm Limits. *Mat. Sci. Semicon. Proc.* **1999**, *2*, 321–327. [[CrossRef](#)]
55. Paredes-Madrid, L.; Matute, A.; Bareño, J.O.; Parra Vargas, C.A.; Gutierrez Velásquez, E.I. Underlying Physics of Conductive Polymer Composites and Force Sensing Resistors (FSRs). A Study on Creep Response and Dynamic Loading. *Materials* **2017**, *10*, 1334. [[CrossRef](#)]
56. Paredes-Madrid, L.; Garzon Posada, A.; Fontalvo, V.; Peña Puerto, A.; Palacio Gómez, C.A. Force Sensing Resistor Data for Enhancing Part-to-Part Repeatability Using a Six Sigma Approach. *IEEE Dataport.* **2021**, *2021*, 16. [[CrossRef](#)]
57. Emara, M.K.; Tomura, T.; Hirokawa, J.; Gupta, S. All-Dielectric Fabry–Pérot-Based Compound Huygens’ Structure for Millimeter-Wave Beamforming. *IEEE Trans. Antennas Propag.* **2021**, *69*, 273–285. [[CrossRef](#)]